Elucidating the Role and Interplay of Nickel and Molybdenum Carbide Particles Supported on Zeolite Y in Methane-Steam Reforming

Xianghui Zhang [a,b], *Di Wu* [a,b,c,d,*], *Su Ha* [b,*]

[a] Alexandra Navrotsky Institute for Experimental Thermodynamics, Washington State University, Pullman, Washington 99163, United States

[b] The Gene and Linda Voiland School of Chemical Engineering and Bioengineering, Washington State University, Pullman, Washington 99163, United States

[c] Department of Chemistry, Washington State University, Pullman, Washington 99163, United States

[d] Materials Science and Engineering, Washington State University, Pullman, Washington 99163, United States

Corresponding Author Email:

Di Wu, *d.wu@wsu.edu*

Su Ha, *suha@wsu.edu*

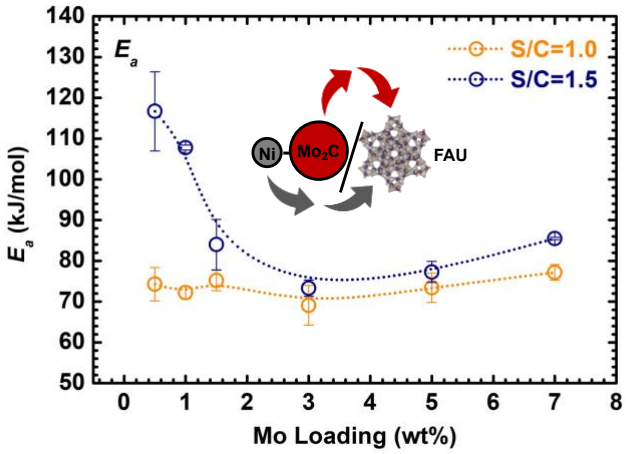

TOC

Abstract

Methane steam reforming (MSR) reaction is a mature industrial process that has been applied for large-scale hydrogen production. Here, we report the synthesis and characterization, reaction kinetics, and deactivation mechanism of a series of catalysts with metallic nickel (Ni) clusters and molybdenum carbide (Mo_2C) particles supported on zeolite Y (Ni-Mo_2C/FAU) in MSR reaction at 850 ^oC. Despite low Ni loading less than 2.4 wt%, MSR on Ni-Mo_2C/FAU exhibits high activity and stability, yet deactivation of Ni-FAU (the sample without Mo_2C) is significant. Further investigations elucidate that the catalyst deactivation is caused by Ni particle sintering via Ostwald ripening instead of coking, and steam induces hydroxylated Ni surface that accelerates sintering. Moreover, encapsulated Mo_2C boosts the activity and stability of Ni on zeolite Y by enhancing CH_4 activation rather than activating H_2O. The interplays among Mo_2C and Ni particles dynamically balance the carbon formation and consumption rates, and inhibit Ni sintering. This study enables insights into an alternative design principle of transition metal carbide – Ni catalysts with high activity and stability for effective MSR by tuning the compositional, structural, and interfacial factors.

Key words: Methane steam reforming (MSR) reaction, metallic nickel (Ni) clusters, molybdenum carbide (Mo_2C), zeolite Y, and sintering.

Introduction

Hydrogen (H_2) is a critical alternative fuel and a clean energy form that plays an important role in closing the global carbon cycle. [1,2] In the current chemical industry and energy infrastructure, the most hydrogen-dependent processes include ammonia synthesis (55%), refinery (25%), and methanol production (10%). [1,2] With high energy efficiency up to 60% and minimized negative environmental impacts, the hydrogen-based fuel cell is potentially another major hydrogen consumption process as we drive to a more sustainable future with hydrogen fuel cell electric vehicles (FCEVs). [3,4] Beyond serving as a critical raw material in the chemical industry, H_2 is also a reducing agent in the metallurgical industry. Therefore, efficient catalytic extraction of hydrogen from water, light hydrocarbons, and other organics where hydrogen is chemically stored, as environmental-friendly fuel in large quantity is an essential and crucial step towards a cleaner future. [5]

Currently, methane steam reforming (MSR) is the dominant industry-scale process to produce H_2. Typical industrial MSR reactions are carried out at 800 ~ 1100 ^oC with pressure between 14 and 40 bar. MSR is a highly endothermic reaction (ΔH_r = 206 kJ/mol), [6] in which high temperature is a favorable reaction condition to yield a high conversion, especially, at high space velocity. The main challenges of such harsh reaction conditions are the coking and sintering of the catalytic Ni-based metallic particles. [7–16] It has been demonstrated that without coking-inhibiting agents, supported Ni catalysts surfer from severe coking in CH_4 activation and decomposition. Thus, synthetical modifications of the Ni sites are necessary to prevent coke formation. Introduction of the second type of metals, such as Ag, Au, Sn, Co, Mo, and Cu, were reported to effectively prevent coking through the formation of alloyed Ni nanoparticles (NPs). [6] The introduced metal atoms typically occupy the step sites of Ni NPs, which feature the highest CH_4 decomposition rate, to effectively inhibit coke formation. In these studies, Ni NPs with loading higher than 8 wt% was supported on α-Al_2O_3, which has

surface areas lower than 10 m^2/g at the high temperature for MSR. [6,17–20] As a result, the abrupt formation of coke at the catalytic sites may quickly reduce the activity, and probably prevent the proper water transport to the catalyst surface, and lead to the uncontrollable growth of carbon filaments. In other words, for effective MSR, supports preserving large surface area with well-dispersed Ni-based catalytic NPs need to be engineered.

Owing to its noble-metal-like physical-chemical properties, Mo_2C has been a popular candidate for heterogeneous catalysis of water–gas shift (WGS) reaction, bio-oil upgrading, and alcohol (methanol and ethanol) steam reforming. [21–24] The common role of Mo_2C in fuel reforming is to prevent coke formation by increasing the activation of oxygenates, such as H_2O and CO_2. Sabnis *et. al.* studied the WGS reaction mechanism of a series of catalysts with transition and noble metals supported on Mo_2C. They concluded that the active sites reside at the metal-Mo_2C interfaces. They also elucidated that for WGS, in reaction at relatively low temperature, the role of Mo_2C is to adsorb and activate H_2O. [25,26] Yao *et. al.* reported activation of H_2O on raft-like Au clusters supported by α-MoC. [27] Shi *et. al.* studied the catalytic role of Ni/Mo_2C with different Ni/Mo ratios in dry reforming of methane (DRM), in which they suggested that the activation of CO_2 is on Mo_2C, and CH_4 activation is on Ni NPs. [28] Hence, it is clear that the high coke-resistant of Mo_2C as support originates from its highly efficient roles in activating oxygenates.

Hydrocarbon activation using Mo_2C requires closely balanced activity – temperature interplays. Past reaction engineering studies mainly concentrated on temperatures lower than 800 ^oC, at which the CH_4 activation on Mo_2C was poor. Recently, Bkour *et. al.* performed CH_4 temperature-programmed reaction (CH_4-TPR) on bulk Mo_2C and unsupported Ni-Mo_2C bimetallic catalysts, in which they found that the onset CH_4 decomposition temperature is around 710 ^oC on Ni-Mo_2C, and is ~900 ^oC on bulk Mo_2C. [29] Using Ni-Mo_2C with different Ni/Mo ratios, Yao *et. al.* further pointed out that the CH_4 decomposition rate in CH_4-TPR

would reach its maximum at temperature higher than 930 °C. [28] These studies suggest promoting role of Mo_2C for Ni-based catalysts in MSR, and as the Mo content varies the temperature and rate of CH_4 decomposition evolve. Moreover, Mo_2C promotes CH_4 decomposition in high-temperature reactions, while it favors H_2O activation at low temperatures.

This study focuses on the catalytic performance, reaction kinetics, and deactivation mechanism of zeolite Y (faujasite, FAU) with internally confined Ni clusters and externally supported Mo_2C particles (Ni-Mo_2C/FAU) in MSR reaction, in which distinctively different roles of Ni NPs and Mo_2C play were elucidated and discussed. Zeolite Y is selected as the support of Ni and Mo_2C species because of its high surface area and effective stabilization of metallic particles and thermal stability at temperatures higher than 800 °C. Our Ni-Mo_2C/FAU catalysts were characterized using *exsitu* X-ray diffraction (XRD), transmission electron microscopy (TEM), and *in situ* CO adsorption diffuse reflectance infrared Fourier transform spectroscopy (DRIFTS). The catalytic performance and kinetics study of MSR over all samples were investigated using a fixed-bed reactor. Further, coupled with thermal analysis with an integrated thermogravimetry–differential scanning calorimetry–mass spectrometry system (TG-DSC-MS) system, we successfully elucidated the deactivation mechanisms, quantified the degree and distribution of coking of spent catalysts after MSR, and distinguished the unique roles of Ni and Mo_2C. Notably, Mo_2C NPs increase the catalytic activity and stability via promoting CH_4 activation instead of H_2O activation. Reaction kinetics with closely balanced CH_4 activation and Ni sintering is necessary to enable MSR with high activity and stability.

Experiment Methods

Material Synthesis

Zeolite NH_4Y (NH_4^+-FAU) with Si/Al ratio = 2.9 was purchased from Alfa Aesar. It was calcined at 500 ^oC in the air for 4 hours to convert it into zeolite HY (FAU). Ion exchange was applied to prepare Ni-exchanged zeolite Y (Ni^{2+}-FAU) from NH_4^+-FAU. Specifically, NH_4^+-FAU (1.00 g) was introduced to $Ni(NO_3)_2$ aqueous solution (0.25 mol/L, 20 mL). This mixture was kept at 50 ^oC for 24 hours under vigorous stirring. Such ion-exchanged process was triplicated to maximize the degree of Ni-exchange. Eventually, the solid product, denoted as Ni^{2+}-FAU, was washed, oven-dried at 100 ^oC overnight, and calcined at 500 ^oC for 4 hours. Ni^{2+}-FAU was reduced in pure H_2 at 700 ^oC for 2 hours, leading to the sample with Ni metal, Ni-FAU. Further, Mo precursor was introduced by incipient wetness impregnation (IWI). Before impregnation, Ni-FAU was pretreated under vacuum at 80 ^oC for 4 hours. Then 1.5 mL ammonia molybdate aqueous solution (0.005 – 0.07 mol/L) was added to 1 gram of Ni-FAU followed by sonication for 1 hour. The product was oven-dried at 100 ^oC overnight, and calcined at 500 ^oC for 4 hours. Finally, the calcined samples were carburized using a temperature programmed method described by Iida *et. al*. Specifically, each calcined sample was carburized in a stream of CH_4/H_2 (15 vol%). The temperature was increased to 300 ^oC at 5 ^oC/min, and to 700 ^oC at 1 ^oC/min, at which carburization lasted for 2 hours. The carburized samples were denoted as Ni-*x*Mo_2C/FAU, in which *x* represents the mass percentage of Mo loading (wt%), ranging from 0.0 to 7.0 wt%.

Sample Characterizations

The composition of each sample was determined using inductively coupled plasma mass spectrometry (ICP-MS). For phase identification, *ex situ* powder X-ray diffraction (XRD) patterns were collected at room temperature between 5 and 60^o (2 ^{o}/min) on a Rigaku Miniflex 600 diffractometer (40 kV, 15 mA, Cu Kα, λ = 0.15418 nm). Transmission electron microscopy (TEM, FEI Tecnai T20, a LaB_6 cathode at 200 kV) was employed to reveal the sample morphology and NP size. Thermal analysis using an integrated TG-DSC-MS system (Netzsch

STA 449 F5 Jupiter coupled with a QMS 403 D Aëolos) was performed to elucidate the coking mechanism. In each measurement, about 20 mg of sample was placed in a platinum (Pt) crucible and analyzed from 30 to 700 °C (10 °C/min) under O_2 flow (10%, 60 mL/min). The evolved gases in TG-DSC analysis were simultaneously identified and quantified by the coupled MS.

In Situ Diffuse Reflectance Infrared Fourier Transform Spectroscopy (In Situ DRIFTS)

In situ diffuse reflectance infrared Fourier transform spectroscopy (*in situ* DRIFTS) analysis was carried out using a high-temperature cell (SpectraTech) with ZnSe windows. Prior to each analysis, 25 mg sample was finely ground and placed in a ceramic crucible. Pretreatment was carried out at 600 ^oC in pure H_2 gas stream for Ni-FAU, and in CH_4/H_2 (15 vol% CH_4) stream at 50 sccm for 30 min for Ni-*x*Mo_2C/FAU. The background spectrum was collected when the cell was cooled down to room temperature under helium (He) flow. In the *in situ* CO adsorption DRIFTS experiments, the carrier gas was switched to pure CO.

Catalytic Performance Test

The catalytic performance of each sample in methane steam reforming (MSR) was tested using a quartz-tube fixed-bed reactor (7-mm). Specifically, the catalyst (~55 mg) was loaded into the reactor with a catalyst bed height of 4 mm. All catalysts were pretreated in CH_4/H_2 stream (15 vol%) at 700 ^oC for 30 minutes. The flow rate of CH_4/H_2 stream was programmed at 20 sccm, and the steam-to-carbon ratios (S/C) were set to be either 1.0 or 1.5. Water vapor was introduced to the reactor via a microsyringe pump at 1.0 mL/h (for the S/C ratio = 1.0) and 1.5 mL/h (for the S/C ratio = 1.5). The evolved products were analyzed using an SRI gas chromatograph equipped with a molecular sieve 13X column, a HayeSep D packed column, and a thermal conductivity detector (TCD). The conversion of CH_4 was calculated

using **Equation (1)**. The yields of H_2, CO, and CO_2 were calculated using **Equations (2)**, **(3)**, and **(4)**, respectively.

$$CH_4\ conversion = \frac{moles\ of\ (CH_{4\ in} - CH_{4\ out})}{moles\ of\ CH_{4\ in}} \qquad Equation\ (1)$$

$$H_2\ yield = \frac{2 \cdot moles\ of\ H_{2\ produced}}{4 \cdot moles\ of\ CH_{4\ in} + 2 \cdot moles\ of H_2O_{in}} \qquad Equation\ (2)$$

$$CO\ yield = \frac{moles\ of\ CO_{produced}}{moles\ of\ CH_{4\ in}} \qquad Equation\ (3)$$

$$CO_2\ yield = \frac{moles\ of\ CO_{2\ produced}}{moles\ of\ CH_{4\ in}} \qquad Equation\ (4)$$

Kinetic Analysis

The reaction kinetics were determined using a fixed-bed reactor containing 25 mg of the catalyst under a feed gas stream of CH_4 (20 sccm) and N_2 (10 sccm) to closely mimic a differential reactor with minimized mass transfer limitation. The conversions were controlled below 10% for the determination of kinetic parameters. All data were recorded at 850 ^oC.

Catalytic Performance Test with CH_4 Pulse Reaction

CH_4 pulse reaction experiments were conducted on all samples using a Diablo 5000A real-time gas analyzer with an Agilent 5975C MSD as a detector. All samples were pre-heated in CH_4/H_2 (15 vol% CH_4) stream from room temperature to 700 ^oC at 10 ^oC/min, and kept at 700 ^oC for 30 minutes for surface oxygen removal. Subsequently, the reaction temperature was increased to 850 ^oC under Ar flow (50 mL/min) before each CH_4 pulse for 10 seconds followed by Ar purge for 3 minutes. The flow rates of CH_4 and Ar were 30 mL/min and 50 mL/min, respectively.

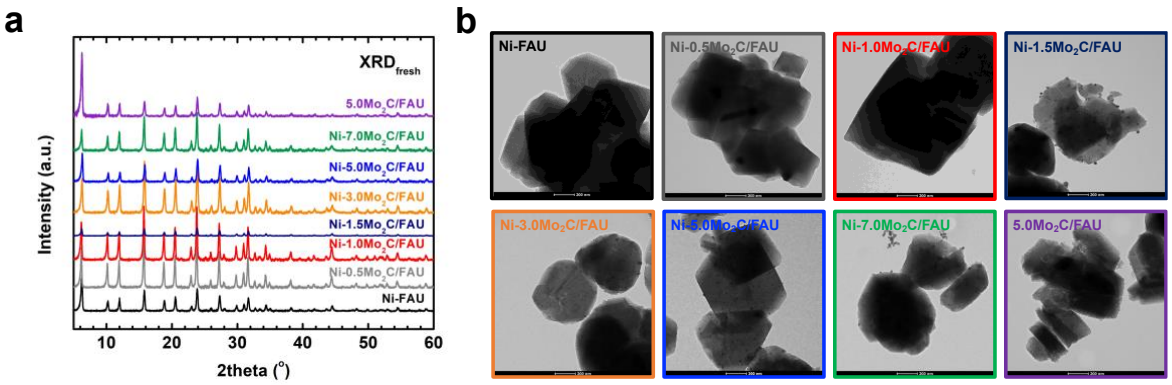

Figure 1. (a) *Ex situ* XRD patterns and **(b)** TEM images of all fresh catalyst samples at room temperature. The sample names are labeled in each image.

Results

ICP-MS data suggest that after ion exchange, the Ni loading is 2.4 wt% for Ni-FAU. The Mo content was determined according to the precursor loading. The XRD patterns plotted in **Figure 1** confirm that all samples retain the cubic structure (*Fd3m*) of zeolite Y after the multistep catalyst synthesis processes. Neither (111) of metallic Ni at 44.5° or (121) of Mo_2C at 39.5° was observed, which suggests that the Ni and Mo_2C particles are "lab X-ray amorphous". The TEM images of Ni-FAU agree well with the structural analysis data. Specifically, there appears to be no detectable NPs on the external surface of Ni-FAU, an indicative of high Ni dispersion within the framework. For Ni-*x*Mo_2C/FAU samples with Mo loading $x < 1.5$, the population of observable NPs on the external surface of FAU is negligible. When $x > 1.5$, more NPs reside externally, and their average NP sizes are ~11.8 nm. The population of NPs increases as the Mo loading increases, yet no detectable particle growth was seen until $x = 7.0$. In other words, when $1.5 \leq x \leq 7.0$, the NPs on Ni-*x*Mo_2C/FAU maintain a constant size of ~11.8 nm. Interestingly, for Mo_2C/FAU, the samples without Ni, no external Mo_2C NP was observed. According to our earlier report, the Mo_2C particles were encapsulated in FAU framework. [30] In addition, by treating the Ni^{2+}-FAU sample under H_2 reduction

atmosphere using the carburization temperature program (**Figure S1a**), and in the carburization stream (15 vol% CH_4/H_2) with the H_2 reduction profile (**Figure S1b**), we confirmed that there was no nickel particle formed in both cases, ruling out the possibility of Ni sintering on the external surface. Consequently, these results indicate that the NPs observed on the external surface of FAU were Mo_2C (see **Figure S1**). Overall, results from XRD and TEM analyses suggest that for Ni-*x*Mo_2C/FAU, the Ni NPs are highly dispersed within the framework, and the Mo_2C NPs observed on the external surface of FAU are also amorphous. Although the number of Mo_2C particles increases as the Mo content increases from 0.5 to 7.0 wt%, all Mo_2C NPs share a constant size of ~11.8 nm. We also noticed that these Mo_2C NPs are amorphous showing no XRD peak (**Figure 1a**). Such phenomenon was not seen in our earlier studies on confinement of MoO_3 and Mo_2C in zeolite HY, [30,31] in which the Mo species stay within the framework, but was observed in multiple studies on synthesis and applications of Mo oxides, carbides, and sulfides supported on zeolites. [32–37]

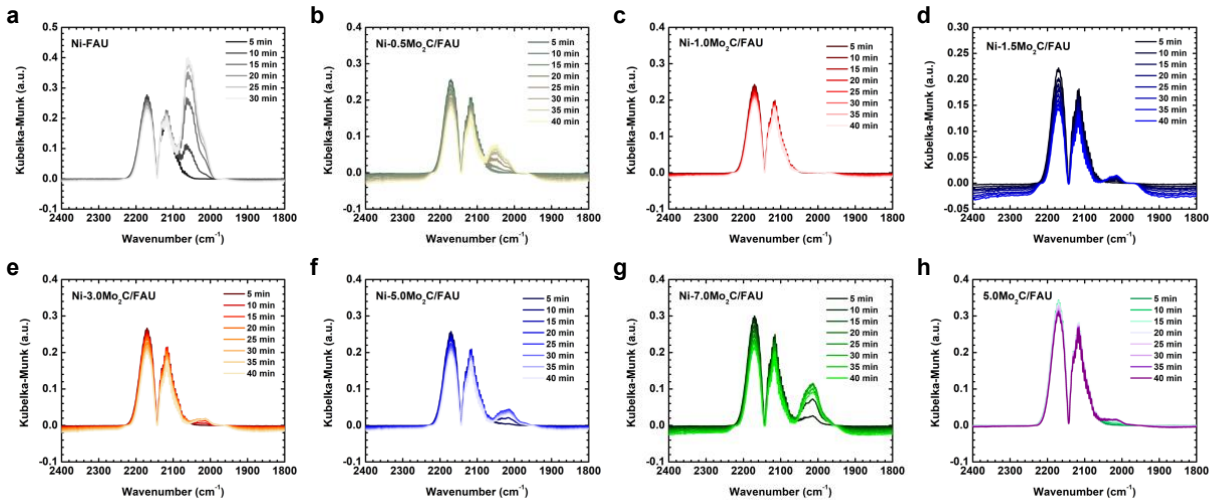

Figure 2. *In situ* CO adsorption DRIFTS results on all fresh catalyst samples at room temperature.

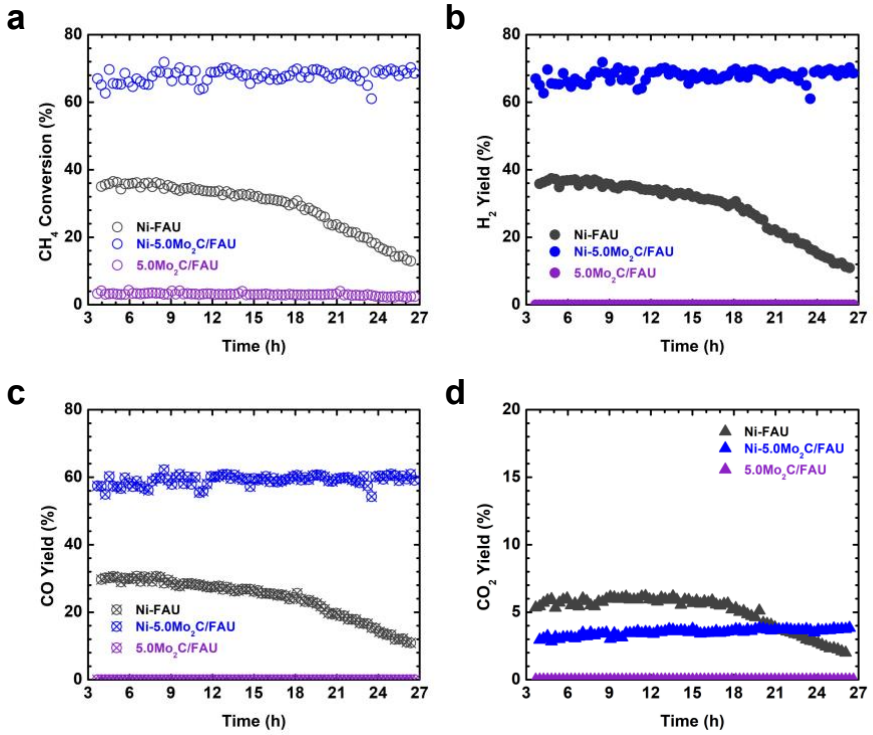

Figure 3. Performance test of Ni-FAU, Ni-5.0Mo_2C/FAU and 5.0Mo_2C/FAU in MSR at 850 °C with 55 mg of catalyst, $F_{methane}$ = 20.3 sccm, S/C = 1.0, and bed height at 0.4 cm.

In situ DRIFTS of CO adsorption experiments were conducted on Ni-FAU and Ni-*x*Mo_2C/FAU to elucidate the electronic structure of encapsulated Ni clusters and the subtle impacts of Mo_2C NPs (see **Figure 2**). As the Mo loading increases, the intensity of adsorbed CO (2060 cm^{-1}) decreases gradually. The lowest intensity was recorded on Ni-1.0Mo_2C/FAU, which presents nearly no evidence of adsorbed CO, while Ni-FAU presents the highest CO adsorption intensity. This indicates that the electron density and distribution of encapsulated Ni^0 clusters are likely modified by the framework-confined Mo_2C particles. Subsequently, for Ni-*x*Mo_2C/FAU with $x \geq 1.5$, a new peak of adsorbed CO at a lower wavenumber of 2020 cm^{-1}, suggesting stronger CO – site binding emerges. Its intensity increases as the Mo_2C loading or *x* increases. In addition, 5.0Mo_2C/FAU presents a peak with lower intensity at 2020 cm^{-1}, confirming this IR signal originates from the stretching vibration of CO adsorbed on Mo_2C particles. Indeed, these two IR peaks are attributed to CO adsorption at the Ni^0 sites (2060 cm^{-1}

[1]) and at the Mo_2C NPs (2020 cm^{-1}). Surprisingly, the CO – Mo_2C binding dominants compared with CO adsorption at Ni^0, strongly suggested by the absence of the peak at 2060 cm^{-1} for Ni-*x*Mo_2C/FAU (*x* = 1.5, 3.0, 5.0 and 7.0) samples with high Mo_2C loading. It is also noticeable that only vibration of linear adsorbed CO (2060 – 2019 cm^{-1}) [38] was detected, no vibration of bridge – bonded CO (1950 -1750 cm^{-1}) [39] was seen on Ni-FAU, which agrees with the structural analysis data and TEM image that Ni^0 is highly dispersed. The *in situ* DRIFTS on CO adsorption results suggest that the electronic structure of Ni within FAU has been impacted by the presence of confined Mo_2C, which leads to the change of its CO binding characteristic on the catalysts.

The catalytic performance of three samples, Ni-FAU, Ni-5.0Mo_2C/FAU, and 5.0Mo_2C/FAU, was evaluated using MSR reaction with the S/C ratio of 1.0 at 850 ^oC for 27 hours (see **Figure 3**). Particularly, Ni-FAU has an initial CH_4 conversion of 35%, which decreases gradually as a function of time-on-stream until reaching 10% at the completion of the 27-hour test. The introduction of Mo_2C significantly increases both catalytic activity and stability. It is highlighted that the initial conversion of CH_4, ~70%, over Ni-5.0Mo_2C/FAU retains till the end of the 27-hour test. Interestingly, despite lower initial CH_4 conversion, H_2 yield, and CO yield of Ni-FAU compared with Ni-5.0Mo_2C/FAU, the CO_2 yield of Ni-FAU is higher than that of Ni-5.0Mo_2C/FAU. Such a phenomenon suggests the existence of a higher O/C ratio on the surface of Ni-FAU. We also noticed that Mo_2C/FAU was not active in MSR (S/C ratio = 1.0) at 850 ^oC. Moreover, the influence of Mo loading on the same catalytic MSR reaction using Ni-*x*Mo_2C/FAU ($0.5 \leq x \leq 7.0$) was investigated (see **Figure S2**). Specifically, although Mo loading has a minor influence on the catalytic activity or stability at S/C = 1.0, a substantial change in performance is seen when the S/C ratio = 1.5 (see **Figure S3**). According to **Figure S3**, the initial activity of all Ni-*x*Mo_2C/FAU samples appears not to be a function of Mo loadings, and presents a shared CH_4 conversion of ~70%. However, for Ni-*x*Mo_2C/FAU

with relatively low Mo loading of 0.5, 1.0 and 1.5 %, the CH_4 conversion decreases significantly to 5% after 25 hours on stream. At x = 3.0, the final CH_4 conversion following the 25-hour test is ~35%. Notably, further increase in Mo loading to 5.0% and 7.0% leads to stable MSR catalyst under the reaction condition with nearly no deactivation throughout the length of tests. Hence, this reaction engineering evidence strongly suggests boosted activity and enhanced stability for Ni-$x$$Mo_2C$/FAU with higher Mo_2C loading in the MSR reaction studied when the higher S/C ratio of 1.5 was used.

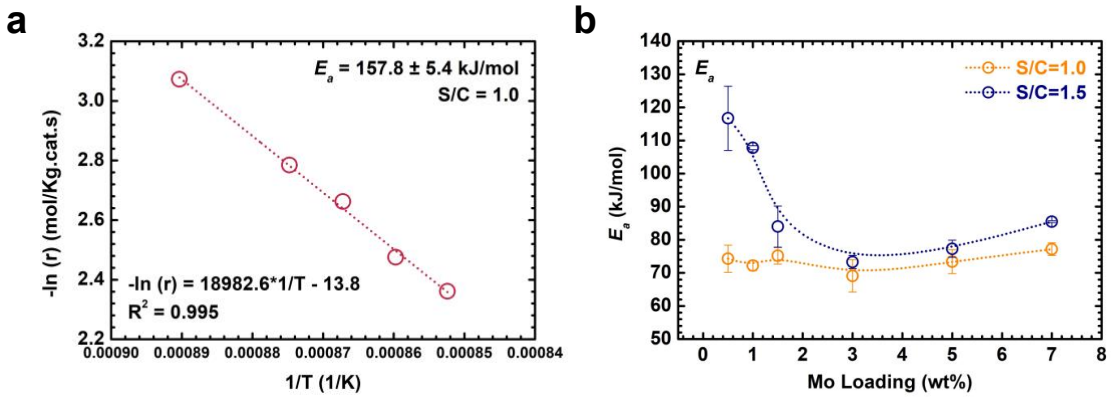

Figure 4. **(a)** The Arrhenius plot of MSR reaction (S/C = 1.0) on Ni-FAU, E_a = 157.8 ± 5.4 kJ/mol, and **(b)** Ni-$x$$Mo_2C$/FAU ($0.5 \leq x \leq 7.0$). "$x$" is the Mo wt%. The MSR reactions were performed on 25 mg of catalyst at 850 ºC with $F_{methane}$ = 20.3 sccm, S/C = 1.0 and 1.5, $F_{nitrogen}$ = 10 sccm and bed height at 0.2 cm.

The activation energies were derived and compared in the kinetic region (see **Figure 4**). Specifically, the E_a is determined to be 157.8 ± 5.4 kJ/mol in MSR catalyzed by Ni-FAU at S/C = 1.0 (**Figure 4a**). However, at S/C = 1.5, E_a cannot be calculated because of the low stability of Ni-FAU catalyst under the given MSR reaction condition. As Mo content increases, the magnitude of E_a systematically evolves (**Figure 4b**). At S/C = 1.0, all Ni-$x$$Mo_2C$/FAU catalysts share similar E_a, approximately 75.0 kJ/mol, and the Mo loading appears not to impact the magnitude of E_a. Interestingly, at S/C = 1.5, the E_a magnitudes decreases from 116.7 kJ/mol to 77.0 kJ/mol as the Mo loading increases from 0.5 Mo-wt% to 3.0 Mo-wt%. It appears that

further increasing the Mo loading beyond 3.0 wt% has no significant effect on the activation energy. Overall, the evolution of E_a as a function of Mo loading and S/C is consistent with the catalytic performance results.

The post-stability-test or spent (*spt*-) samples were examined by XRD and TEM for phase and morphological evaluations, respectively (see **Figure 5**). Generally, all samples retain the cubic FAU (*Fd3m*) structure of zeolite Y except *spt*-5Mo_2C/FAU, which shows detectable evidence of framework degradation (see **Figure 1a** and **5a**). Interestingly, a new diffraction peak emerges at 39.5 ^{o} on the spent samples with Mo loading higher than 3.0 %. This peak belongs to the (121) reflection of Mo_2C, which is likely to be a product of sintering and crystallization of the "X-ray amorphous" particles under harsh MSR reaction condition. Similar phenomena were also observed in multiple studies on Mo species under support, by Joshua *et. al.* on MoP at above 600 ^{o}C, and by Okuyama *et. al.* in growing Mo_2C particles from its amorphous phase via ion bombardment. [36,37] The TEM images reveal that sintering is a shared phenomenon for all samples. More specifically, Ni NPs (~96.7 nm) were observed on the external surface of *spt*-Ni-FAU. On the external surface of all *spt*-Ni-*x*Mo_2C/FAU samples, the particle size increases and distribution widens compared with corresponding fresh Ni-*x*Mo_2C/FAU, and the particles detected are much smaller than Ni particles on *spt*-Ni-FAU. In addition, the amount of external surface carbon increases as the Mo loading increases (see **Figure 5b**). It is found that below 3.0 Mo-wt%, no filament carbon is detected, while it increasingly builds up as the Mo content increases to 7.0 Mo-wt%. Hence, the Mo_2C in *spt*-Ni-*x*Mo_2C/FAU promotes CH_4 activation. We also noticed that there appears to be no filament carbon on *spt*-5.0Mo_2C/FAU, the sample without Ni.

To quantify the coke formation and coking site distribution, TPO experiments using integrated TG-DSC-MS were performed on each *spt*-sample (see **Figure 6**). TPO results suggest that thermal oxidation of spt-samples is stepwise with two major stages. In *Stage I*, TG

weight loss levels at temperature below 300 °C, which is primarily owing to endothermic dehydration evidenced by DSC and MS curves (m/z = 18, see **Figure 6b** and **c**). Within *Stage I*, no detectable CO_2 signal was recorded by MS (**Figure 6d**). In *Stage II*, the coke (carbon) decomposition in oxidative atmosphere starts at about 400 °C, which leads to significantly exothermic DSC peaks due to combustion spanning from ~400 to 700 °C (see **Figure 6b** and **d**). In this process, CO_2 (m/z = 44) is released, using which we are able to quantify the coke on each *spt*-sample. Specifically, the coke contents are 0.40 % for Ni-FAU and 4.6 % for 5.0Mo_2C/FAU. The general trend is that as the Mo content increases the degree of coking increases, and highest coke load was seen on Ni-7.0Mo_2C/FAU (~4.3%). Moreover, at Mo loading higher than 3.0, we were able to distinguish the "light coke" (C_L) centered at about 540 °C, and the "hard coke" (C_H) peaked at about 580 °C. Particularly, the C_L : C_H ratio is approximately 1 : 2 for Ni-3.0Mo_2C/FAU, 2 : 1 for Ni-5.0Mo_2C/FAU, and 3 : 1 for Ni-7.0Mo_2C/FAU. The C_L : C_H ratio of 5.0Mo_2C/FAU is ~ 3.5 : 1. Such coke distribution suggests at least two types of coke with different binding strength at the active sites exist, and as the Mo_2C content increases, the percentage of C_L increases. Therefore, consistent results from TEM and thermal analysis confirm that the presence of Mo_2C NPs promotes CH_4 activation in MSR reaction evidenced by the increased degree of coke formation as more Mo_2C introduced.

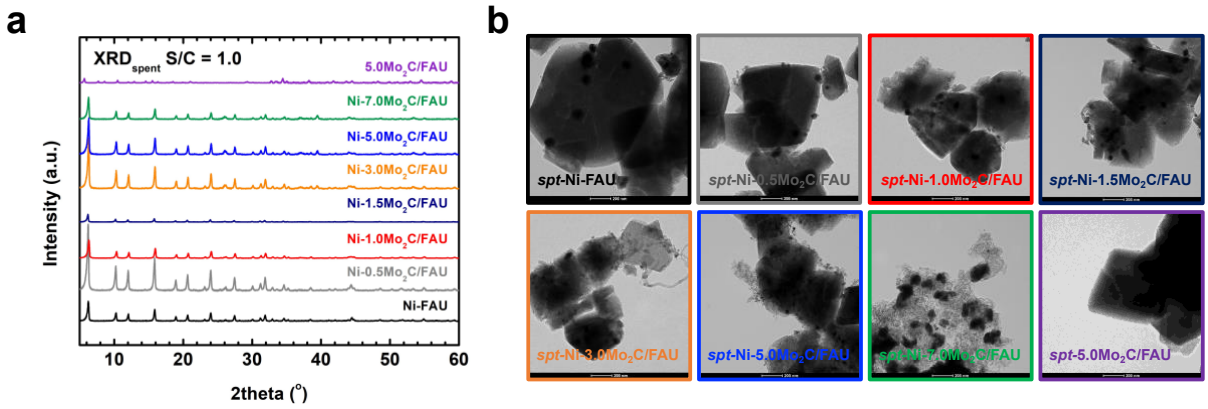

Figure 5. (a) *Ex situ* XRD patterns at room temperature and **(b)** TEM images of all spent catalyst samples after MSR at 850 °C with 55 mg of catalyst, $F_{methane}$ = 20.3 sccm, S/C = 1.0, and bed height at 0.4 cm.

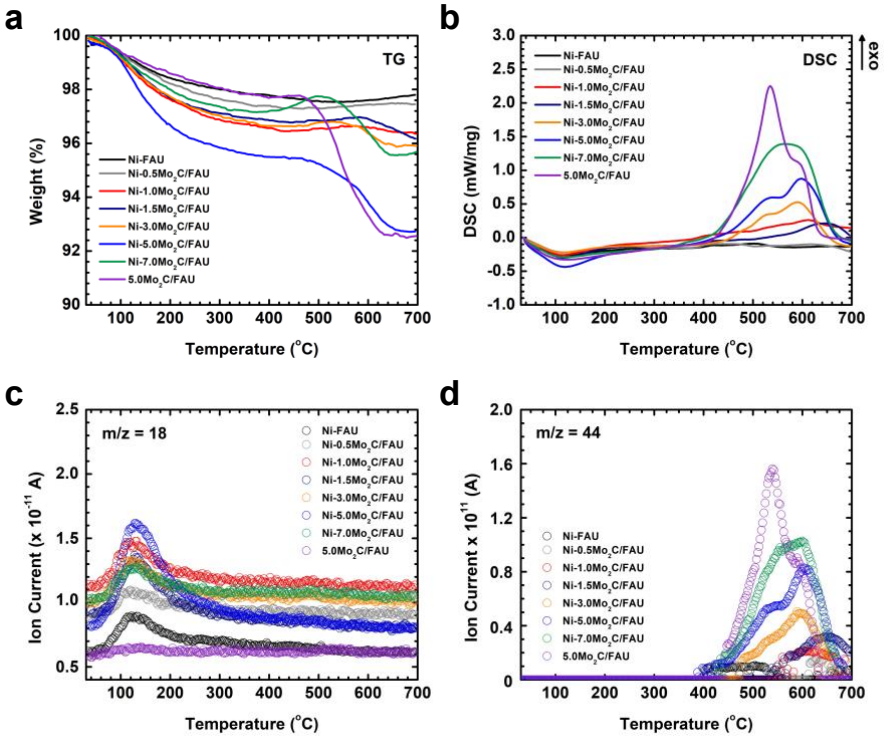

Figure 6. TPO results of all spent catalyst samples after MSR on 55 mg of catalysts at 850 °C with $F_{methane}$ = 20.3 sccm, S/C = 1.0, and bed height at 0.4 cm. **(a)** TG, **(b)** DSC, **(c)** MS of H_2O (m/z =18), and **(d)** MS of CO_2 (m/z =44). These TPO experiments were carried out using an integrated TG-DSC-MS system 30 to 700 °C (10 °C/min) under O_2 flow (10%, 60 mL/min).

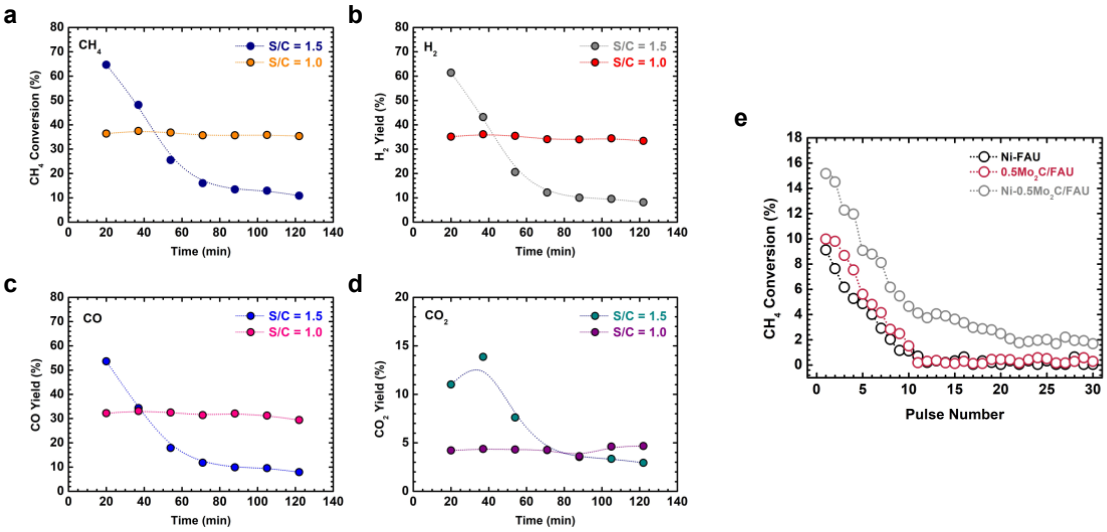

Figure 7. Performance test of Ni-FAU in MSR at 850 °C with S/C = 1.0 and 1.5. **(a)** CH_4 conversion, **(b)** H_2 yield, **(c)** CO yield and **(d)** CO_2 yield. The MSR reactions were performed on 55 mg of catalyst at 850 °C with $F_{methane}$ = 20.3 sccm, S/C = 1.0 and 1.5, and bed height at 0.4 cm. **(e)** CH_4 conversion results of methane pulse reaction over Ni-FAU, Ni-0.5Mo_2C/FAU, and 0.5Mo_2C/FAU samples at 850 °C.

Ni-FAU Deactivation Mechanisms

To further elucidate the exact deactivation mechanism of Ni-FAU, and to reveal the role of Mo_2C, we first examined the MSR performance of Ni-FAU at 850 ^oC at S/C = 1.0 and 1.5 (see **Figure 7**). Typically, the two catalytic deactivation mechanisms in MSR, (i) coking and (ii) sintering, respond differently as a function of the S/C ratio. Once coking dominants, a higher S/C ratio results in better catalytic stability owing to promoted carbon consumption rate. When sintering is responsible for deactivation, the S/C ratio increase leads to higher surface OH group concentration, at which particle sintering is favorable. Our experimental observation is that at S/C = 1.0, Ni-FAU is catalytically stable within a range of tests we performed showing nearly consistent CH_4 conversion, while at S/C = 1.5 its stability significantly decreases from 65% to ~10% within 90 minutes. Most existing reports suggest although higher S/C inhibit coking, the presence of steam promotes sintering of Ni NPs in MSR, resulting in catalyst deactivation. For example, Bartholomew *et. al.* reviewed the sintering kinetics of Ni in pure H_2 and 3%H_2O (steam)/H_2 atmosphere at temperatures ranging from 630 to 830 ^oC. [40] They pointed out that at a given temperature, in steam, the rate of Ni NP sintering was significantly higher compared with the rate under dry conditions. Parallelly, coupling experimental reaction kinetic and DFT computational methods, Sehested *et. al.* reported that above 700 ^oC the sintering rate of Ni NPs deviated from the particle migration and coalescence models, yet their data fit Ostwald ripening well. [41] They further proposed that the Ni_2-OH clusters, which have a diffusion rate 700 times higher than that of Ni atoms, were likely responsible for the quick sintering of Ni in MSR.

Based on the strong metal – support interaction, it is considered that smaller Ni particles dispersed over the high surface area support can show the increased activity with the improved resistance to sintering. Ostwald ripening, a thermodynamically driven particle growth process governed by Ni – Ni inter-particle interactions, has not been typically considered. To harness

Ostwald ripening under the presence of steam or simply water, the formation of hydroxylated Ni surface with Ni_2-OH intermediates, has to be well-controlled through subtly balanced the hydroxylation and carbon activation at the reactants – catalyst interfaces. Recently, Li *et. al.* studied the coke formation on Ni/ZrO_2 as a function of Ni content. [42] It was found that both reforming activity and coke selectivity increased as the Ni loading increased. In other words, catalysts with low Ni loading are supposed to have low MSR activity. For instance, Xu *et. al.* and Cui *et. al.* further investigated the rate of CH_4 decomposition on Ni/Al_2O_3 with different Ni particle sizes, achieved by altering Ni loading. [43,44] It was found that between 7.0 and 39.7 nm the initial turnover frequency (TOF) increased as a function of Ni particle size, and the maximum TOF was obtained when the average size of Ni NPs is 31.8 nm. In this study, according to the ICP-MS results, the Ni contents of the Ni-*x*Mo_2C/FAU samples are all less than 2.4 wt%, within the range where the CH_4 decomposition rate decreases as the Ni particle size decreases. In this region of the Ni particle size, the CH_4 decomposition rate on Ni-FAU is considerably low. On one hand, both the TEM images and TPO results are in excellent agreement with these studies by further confirming that Ni-FAU deactivation in MSR is primarily caused by sintering of Ni NPs instead of coking; the low CH_4 activity of Ni-FAU is responsible for its fast sintering rate. On the other hand, multiple evidence points out that the co-existed Mo_2C particles on our Ni-xMo_2C/FAU catalysts with significantly lower Ni loading must play critical roles in preventing Ni sintering in MSR, leading to enhanced catalytic activity and stability.

Roles of Mo_2C Particles in MSR on Ni-xMo_2C/FAU

To boost the MSR activity, Mo_2C is supposed to increase the CH_4 activation at the Ni sites, which is the rate-limiting step of MSR on Ni-FAU. The performance test data in **Figure 3** suggest that introduction of Mo_2C to Ni-FAU enhances both catalytic activity and stability in MSR. In **Figures 5** and **6**, the TEM images and TPO results suggest a higher degree of

coking on *spt*-Ni-5.0Mo_2C/FAU (3.4 wt%) compared with that on *spt*-Ni-FAU (0.4 wt%). Introduction of Mo_2C to Ni-FAU significantly decreases E_a from 157.8 kJ/mol for Ni-FAU to 75 kJ/mol for Ni-5.0Mo_2C/FAU, leading to much faster CH_4 activation/decomposition kinetics (see **Figure 3**). On the other hand, without Ni pre-loaded, 5.0Mo_2C/FAU is not active in MSR at 850 ^oC with no CH_4 conversion detected. We notice that in TPO data, the coke formed on *spt*-5.0Mo_2C/FAU (4.6 wt%) is higher than those of all *spt*-Ni-5.0Mo_2C/FAU samples (see **Figure 6**). Such phenomenon indicates that (i) CH_4 activation on Mo_2C is faster than the carbon consumption rate at S/C = 1.0, and (ii) Mo_2C NP itself on 5.0Mo_2C/FAU is MSR-inactive due to the formation of coated carbon.

For quantitative confirmation of CH_4 activation increase after the introduction of Mo_2C onto Ni-FAU, we carried out CH_4 pulse reaction at 850 ^oC on Ni-FAU, Ni-0.5Mo_2C/FAU, and 0.5Mo_2C/FAU samples (see **Figure 7e**). The initial conversions of CH_4 over Ni-FAU, Ni-0.5Mo_2C/FAU, and 0.5Mo_2C/FAU samples are 9%, 15%, and 10%, respectively. This provides further confirmation that the significant increase in the CH_4 activation rate observed here is tightly related to Mo_2C loading. In addition, although virtually, the CH_4 conversions over Ni-FAU and 0.5Mo_2C/FAU are quite similar, considering $Ni_{(Ni\text{-}FAU)}$: $Mo_{(0.5Mo2C/FAU)}$ = ~ 4 (i.e., 4 times more weight of Ni was used for Ni-FAU than Mo used for 0.5Mo_2C/FAU), the mass-based CH_4 activation activity on 0.5Mo_2C/FAU is indeed approximately 4 times higher than that of Ni-FAU. Hence, the CH_4 pulse test results further assure that Mo_2C introduction significantly promotes the CH_4 decomposition rate of Ni-*x*Mo_2C/FAU catalysts.

The role of Mo_2C was further studied with MSR reaction as a function Mo loading at S/C ratio = 1.0 and 1.5 at 850 ^oC. Specifically, at S/C ratio = 1.0, the Mo_2C on Ni-*x*Mo_2C/FAU has nearly no influence in MSR, and the conversion of CH_4 is in a narrow range, between 65% and 70%, with E_a = 75 kJ/mol. Meanwhile, the TPO results of spent samples show increased coke formation as more Mo is added, which suggests a higher rate of CH_4 activation on Ni sites

as a function of Mo loading. Earlier, for the family of catalysts studied here, we proposed that faster CH_4 activation kinetics tolerate high S/C ratio operating conditions by balancing the excess steam and preventing Ni oxidation. To test our hypothesis, we carried out MSR reactions on Ni-*x*Mo_2C/FAU samples at S/C ratio = 1.5. Interestingly, we noticed that in the 25-hour test, only Ni-5.0Mo_2C/FAU and Ni-7.0Mo_2C/FAU retained their high activity, while for samples with Mo lower than 5.0wt%, the activity gradually decreased. We also noticed that the Mo_2C particles of all spent samples, especially *spt*-Ni-7.0Mo_2C/FAU, are decorated/coated by carbon filament. Such a phenomenon suggests the rate of coke formation is faster than the carbon consumption rate at S/C = 1.0. Therefore, a higher S/C ratio is desired for samples with high Mo loading for balanced interplays between interfacial coke formation and carbon consumption. This explains why at S/C ratio = 1.5, the catalytic stability is significantly improved for Ni-*x*Mo_2C/FAU samples with high Mo loading, at 5% and 7wt%. In contrast, at Mo loading lower than 5wt% and at S/C ratio = 1.0, only a small amount of coke was detected on the spent samples. Consequently, the catalytic activity for MSR on these Ni-*x*Mo_2C/FAU samples significantly decreases at S/C ratio = 1.5 due to the excess amount of steam that cannot be balanced out by its slow CH_4 activity.

Distribution of Mo_2C Species on Ni-xMo_2C/FAU – "Internally Confined Mo_2C Clusters v.s. Externally Supported Mo_2C Nanoparticles"

Direct experimental results suggest that the metallic Ni clusters are confined in FAU, and Mo_2C NPs (~11.8 nm) are on the external of FAU. Moreover, multiple evidences strongly support the presence of internally confined/encapsulated Mo_2C clusters within the FAU framework assisting the Ni clusters to enhance the MSR reaction. *First*, the catalytic performance test results point out that without co-existed metallic Ni, the sample 5.0Mo_2C/FAU, presents no MSR activity (see **Figure 3**). Meanwhile, when the external Mo_2C NPs are severely coked, the MSR performance on both Ni-5.0Mo_2C/FAU and Ni-

7.0Mo_2C/FAU is not impacted. This suggests that the enhanced MSR performance on Ni-5.0Mo_2C/FAU is because of the interplays between encapsulated Ni and Mo_2C clusters in FAU, and is not due to CH_4 activation on externally supported Mo_2C NPs. *In addition*, the compositional analysis by ICP-MS elucidates that the Ni content of Ni-FAU synthesized is 2.4 wt%. In other words, at such a low Ni loading, the degree of ion-exchanged for Ni^{2+}-FAU is merely 36.4%, which facilitates the introduction of well-dispersed Mo_2C clusters confined in FAU, evidenced by the TEM images of 5.0Mo_2C/FAU in **Figure 1b**, and supported by our recent publication on Mo_2C/FAU formation energetics. [30] *Furthermore*, thse encapsulated Mo_2C clusters in FAU are very active in CH_4 decomposition, suggested by the CH_4 pulse decomposition data of 0.5Mo_2C/FAU, and reflected by the TPO results of *spt*-5Mo_2C/FAU (**Figures 6** and **7**). Therefore, the enhanced MSR performance seen on Ni-5.0Mo_2C/FAU is not owing to CH_4 activation on Mo_2C NPs located at the external surface of FAU. Instead, the enhanced activity belongs to the well-dispersed Ni metal clusters encapsulated in the microporosity of zeolite Y, which have also been stabilized chemically by the internally confined Mo_2C species. Unlike the Mo_2C NPs located at the external surface of FAU, these dispersed Mo_2C species are different in that they are located close to Ni clusters within the cage structure of FAU. Specifically, the *in situ* CO adsorption DRIFTS data strongly suggest that the electronic structure of these Ni clusters has been perturbed by Mo_2C (see **Figure 4**). Hence, the introduction of Mo_2C significantly improves the activity and stability of Ni-FAU in MSR reaction by boosting the CH_4 activation rate at Ni, and the active sites are Mo_2C-promoted Ni clusters primarily in the FAU framework.

Conclusions

In this study, we designed and synthesized a family of catalysts with tuned Ni and Mo_2C supported on zeolite Y (FAU) for gas-phase catalytic MSR at 850 ^oC. After systematic material characterizations, MSR performance tests, and reaction kinetics studies, we successfully

elucidated the (i) deactivation mechanism of Ni sites, (ii) the promoting role of encapsulated/confined Mo_2C on both catalytic activity and stability. First of all, the deactivation of metallic Ni sites features a highly dynamic mechanism with two competing factors, namely, Ni particle sintering and CH_4 activation at the Ni sites. Because of its low activation activity towards CH_4 in MSR, the surface of Ni particles is hydroxylated, which results in energetically favorable particle affinity resulting in fast sintering. We also point out that encapsulated/confined Mo_2C promotes MSR reaction by taking advantage of its strong capability in CH_4 activation, evidenced by the positively correlated Mo loadings and degree of coking. Thus, integration of Ni and Mo_2C on FAU enhances CH_4 activation, inhibits Ni hydroxylation, and balances the rates of carbon formation and consumption, which enables increased catalyst stability. We further deduce that the existence of *external* Mo_2C NPs and the coke formed around them may likely increase the overall hydrophobicity of the Ni-*x*Mo_2C/FAU NPs. Currently, we are testing this using water vapor adsorption calorimetry to reveal the hydration energetics of Ni-*x*Mo_2C/FAU as a function of vapor partial pressure. We'll report these calorimetric results separately in subsequent publications.

Acknowledgement

This work was supported by institutional funds from the Gene and Linda Voiland School of Chemical Engineering and Bioengineering and Alexandra Navrotsky Institute for Experimental Thermodynamics at Washington State University. Xianghui Zhang is supported by Chambroad Distinguished Scholarship.

Associated Content

Supporting Information

The *Supporting Information* is available free of charge at

https://pubs.acs.org/doi/10.1021/acs.xxx.xxxxxxx

The details of additional TEM images, and reaction engineering data.

Author Information

Corresponding Authors

Di Wu − Alexandra Navrotsky Institute for Experimental Thermodynamics, Voiland School of Chemical Engineering and Bioengineering, Department of Chemistry, and Materials Science and Engineering, Washington State University, Pullman, Washington 99164, United States; orcid.org/0000-0001- 6879-321X; Email: d.wu@wsu.edu

Su Ha – Voiland School of Chemical Engineering and Bioengineering, Washington State University, Pullman, Washington 99164, United States; Email: suha@wsu.edu

Authors

Xianghui Zhang − Alexandra Navrotsky Institute for Experimental Thermodynamics and Voiland School of Chemical Engineering and Bioengineering, Washington State University, Pullman, Washington 99164, United States

References

(1) Momirlan, M.; Veziroglu, T. N. Current Status of Hydrogen Energy. *Renew. Sustain. Energy Rev.* **2002**, *6*, 141–179. https://doi.org/10.1016/S1364-0321(02)00004-7.

(2) Edwards, P. P.; Kuznetsov, V. L.; David, W. I. Hydrogen Energy. *Philos. Trans. R. Soc. A Math. Phys. Eng. Sci.* **2007**, *365*, 1043–1056. https://doi.org/10.1098/rsta.2006.1965.

(3) Tanç, B.; Arat, H. T.; Baltacıoğlu, E.; Aydın, K. Overview of the next Quarter Century Vision of Hydrogen Fuel Cell Electric Vehicles. *International Journal of Hydrogen Energy*. 2019, pp 10120–10128. https://doi.org/10.1016/j.ijhydene.2018.10.112.

(4) Eriksson, E. L. V.; Gray, E. M. A. Optimization and Integration of Hybrid Renewable Energy Hydrogen Fuel Cell Energy Systems – A Critical Review. *Applied Energy*. 2017, pp 348–364. https://doi.org/10.1016/j.apenergy.2017.03.132.

(5) Hanley, E. S.; Deane, J. P.; Gallachóir, B. P. Ó. The Role of Hydrogen in Low Carbon Energy Futures–A Review of Existing Perspectives. *Renewable and Sustainable Energy Reviews*. 2018, pp 3027–3045. https://doi.org/10.1016/j.rser.2017.10.034.

(6) Meloni, E.; Martino, M. A Short Review on Ni Based Catalysts and Related Engineering Issues for Methane Steam Reforming. *Catalysts* **2020**, *10* (3), 352.

(7) Wang, Z.; Cao, X. M.; Zhu, J.; Hu, P. Activity and Coke Formation of Nickel and Nickel Carbide in Dry Reforming: A Deactivation Scheme from Density Functional Theory. *J. Catal.* **2014**, *311*, 469–480. https://doi.org/10.1016/j.jcat.2013.12.015.

(8) Trimm, D. L. Coke Formation and Minimisation during Steam Reforming Reactions. *Catal. Today* **1997**, *37* (3), 233–238. https://doi.org/10.1016/S0920-5861(97)00014-X.

(9) Christensen, K. O.; Chen, D.; Lødeng, R.; Holmen, A. Effect of Supports and Ni Crystal Size on Carbon Formation and Sintering during Steam Methane Reforming. *Appl. Catal. A Gen.* **2006**, *314* (1), 9–22. https://doi.org/10.1016/j.apcata.2006.07.028.

(10) Liu, C. J.; Ye, J.; Jiang, J.; Pan, Y. Progresses in the Preparation of Coke Resistant Ni-Based Catalyst for Steam and CO_2 Reforming of Methane. *ChemCatChem* **2011**, *3* (3), 529–541. https://doi.org/10.1002/cctc.201000358.

(11) Zhang, Y.; Wang, W.; Wang, Z.; Zhou, X.; Wang, Z.; Liu, C.-J. Steam Reforming of Methane over Ni/SiO_2 Catalyst with Enhanced Coke Resistance at Low Steam to Methane Ratio. *Catal. Today* **2015**, *256*, 130–136.

(12) Nieva, M. A.; Villaverde, M. M.; Monzón, A.; Garetto, T. F.; Marchi, A. J. Steam-Methane Reforming at Low Temperature on Nickel-Based Catalysts. *Chemical Engineering Journal*. 2014, pp 158–166. https://doi.org/10.1016/j.cej.2013.09.030.

(13) Teixeira, A. C. S. C.; Giudici, R. Deactivation of Steam Reforming Catalysts by Sintering: Experiments and Simulation. *Chem. Eng. Sci.* **1999**, *54* (15–16), 3609–3618. https://doi.org/10.1016/S0009-2509(98)00516-8.

(14) Bartholomew, C. H. Sintering Kinetics of Supported Metals: New Perspectives from a Unifying GPLE Treatment. *Appl. Catal. A, Gen.* **1993**, *107* (1), 1–57. https://doi.org/10.1016/0926-860X(93)85114-5.

(15) Hansen, T. W.; Delariva, A. T.; Challa, S. R.; Datye, A. K. Sintering of Catalytic Nanoparticles: Particle Migration or Ostwald Ripening? *Acc. Chem. Res.* **2013**, *46* (8), 1720–1730. https://doi.org/10.1021/ar3002427.

(16) Sehested, J.; Carlsson, A.; Janssens, T. V. W.; Hansen, P. L.; Datyey, A. K. Sintering of Nickel Steam-Reforming Catalysts on $MgAl_2O_4$ Spinel Supports. *J. Catal.* **2001**, *197* (1), 200–209. https://doi.org/10.1006/jcat.2000.3085.

(17) Boudjeloud, M.; Boulahouache, A.; Rabia, C.; Salhi, N. La-Doped Supported Ni Catalysts for Steam Reforming of Methane. *Int. J. Hydrogen Energy* **2019**, *44* (20), 9906–9913. https://doi.org/10.1016/j.ijhydene.2019.01.140.

(18) Lertwittayanon, K.; Youravong, W.; Jye, W. Enhanced Catalytic Performance of Ni/a-Al_2O_3 Catalyst Modified with $CaZrO_3$ Nanoparticles in Steam-Methane Reforming. *Int. J. Hydrogen Energy* **2017**, *42* (47), 28254–28265. https://doi.org/10.1016/j.ijhydene.2017.09.030.

(19) Morales-cano, F.; Lundegaard, L. F.; Tiruvalam, R. R.; Falsig, H.; Skjøth-rasmussen, M. S. Improving the Sintering Resistance of Ni/Al_2O_3 Steam-Reforming Catalysts by Promotion with Noble Metals. *Applied Catal. A, Gen.* **2015**, *498*, 117–125. https://doi.org/10.1016/j.apcata.2015.03.016.

(20) Pashchenko, D. Experimental Investigation of Reforming and Flow Characteristics of a Steam Methane Reformer Filled with Nickel Catalyst of Various Shapes. *Energy Convers. Manag.* **2019**, *185*, 465–472. https://doi.org/10.1016/j.enconman.2019.01.103.

(21) Environ, E.; Chen, Z.; Higgins, D.; Yu, A.; Zhang, J. A Review on Non-Precious Metal Electrocatalysts for PEM Fuel Cells. *Energy Environ. Sci.* **2011**, *4*, 3167–3192. https://doi.org/10.1039/c0ee00558d.

(22) Cheekatamarla, P. K.; Finnerty, C. M. Reforming Catalysts for Hydrogen Generation in Fuel Cell Applications. *J. Power Sources* **2006**, *160*, 490–499. https://doi.org/10.1016/j.jpowsour.2006.04.078.

(23) Ma, Y.; Guan, G.; Hao, X.; Cao, J.; Abudula, A. Molybdenum Carbide as Alternative Catalyst for Hydrogen Production – A Review. *Renew. Sustain. Energy Rev.* **2017**, *75*, 1101–1129. https://doi.org/10.1016/j.rser.2016.11.092.

(24) Levalley, T. L.; Richard, A. R.; Fan, M. The Progress in Water Gas Shift and Steam Reforming Hydrogen Production Technologies - A Review. *Int. J. Hydrogen Energy* **2014**, *39* (30), 16983–17000. https://doi.org/10.1016/j.ijhydene.2014.08.041.

(25) Sabnis, K. D.; Cui, Y.; Akatay, M. C.; Shekhar, M.; Lee, W.; Miller, J. T.; Delgass, W. N.; Ribeiro, F. H. Water – Gas Shift Catalysis over Transition Metals Supported on Molybdenum Carbide. *J. Catal.* **2015**, *331*, 162–171. https://doi.org/10.1016/j.jcat.2015.08.017.

(26) Sabnis, K. D.; Akatay, M. C.; Cui, Y.; Sollberger, F. G.; Stach, E. A.; Miller, J. T.; Delgass, W. N.; Ribeiro, F. H. Probing the Active Sites for Water – Gas Shift over Pt/Molybdenum Carbide Using Multi-Walled Carbon Nanotubes. *J. Catal.* **2015**, *330*, 442–451. https://doi.org/10.1016/j.jcat.2015.07.032.

(27) Yao, S.; Zhang, X.; Zhou, W.; Gao, R.; Xu, W.; Ye, Y.; Lin, L. Atomic-Layered Au Clusters on α-MoC as Catalysts for the Low-Temperature Water-Gas Shift Reaction. *Science.* **2017**, *393*, 389–393.

(28) Shi, C.; Zhang, A.; Li, X.; Zhang, S.; Zhu, A.; Ma, Y.; Au, C. Ni-Modified Mo_2C Catalysts for Methane Dry Reforming. *Appl. Catal. A, Gen.* **2012**, *432*, 164–170. https://doi.org/10.1016/j.apcata.2012.04.035.

(29) Bkour, Q.; Marin-flores, O. G.; Norton, M. G.; Ha, S. A Highly Active and Stable Bimetallic Ni-Mo_2C Catalyst for a Partial Oxidation of Jet Fuel. *Appl. Catal. B Environ.* **2019**, *245*, 613–622. https://doi.org/10.1016/j.apcatb.2019.01.027.

(30) Zhang, X.; Reece, M. E.; Cockreham, C. B.; Sun, H.; Wang, B.; Xu, H.; Sun, J.; Guo, X.; Su, H.; Wang, Y. Formation Energetics and Guest—Host Interactions of Molybdenum Carbide Confined in Zeolite Y. *Ind. Eng. Chem. Res.* **2021**, *60*, 13991–14003. https://doi.org/10.1021/acs.iecr.1c02822.

(31) Zhang, X.; Strzelecki, A. C.; Cockreham, C. B.; Goncharov, V. G.; Li, H.; Sun, J.; Sun, H.; Guo, X.; Xu, H.; Su, H.; et al. Thermodynamics of Molybdenum Trioxide (MoO_3) Encapsulated in Zeolite Y. *AIChE J.* **2021**, 1–20. https://doi.org/10.1002/aic.17464.

(32) Nagai, M.; Zahidul, A.; Matsuda, K. Nano-Structured Nickel – Molybdenum Carbide Catalyst for Low-Temperature Water-Gas Shift Reaction. *Appl. Catal. A, Gen.* **2006**, *313*, 137–145. https://doi.org/10.1016/j.apcata.2006.07.006.

(33) Nagai, M.; Matsuda, K. Low-Temperature Water – Gas Shift Reaction over Cobalt – Molybdenum Carbide Catalyst. *J. Catal.* **2006**, *238*, 489–496. https://doi.org/10.1016/j.jcat.2006.01.003.

(34) Du, C.; Yan, B.; Yang, G. Nano Energy Self-Integrated Effects of 2D $ZnIn_2S_4$ and Amorphous Mo_2C Nanoparticles Composite for Promoting Solar Hydrogen Generation. *Nano Energy* **2020**, *76*, 105031. https://doi.org/10.1016/j.nanoen.2020.105031.

(35) Tran, P. D.; Tran, T. V; Orio, M.; Torelli, S.; Truong, Q. D.; Nayuki, K.; Sasaki, Y.; Chiam, S. Y.; Yi, R.; Honma, I.; et al. Coordination Polymer Structure and Revisited Hydrogen Evolution Catalytic Mechanism for Amorphous Molybdenum Sulfid. *Nat. Mater.* **2016**, *15*, 640–647. https://doi.org/10.1038/NMAT4588.

(36) McEnaney, J. M.; Chance Crompton, J.; Callejas, J. F.; Popczun, E. J.; Biacchi, A. J.; Lewis, N. S.; Schaak, R. E. Amorphous Molybdenum Phosphide Nanoparticles for Electrocatalytic Hydrogen Evolution. *Chem. Mater.* **2014**, *26* (16), 4826–4831. https://doi.org/10.1021/cm502035s.

(37) Okuyama, F.; Fujimoto, Y.; Kato, S.; Kondo, T. Growth of Molybdenum Carbide Particles from an Amorphous Phase Induced by Ion Bombardment. *Appl. Phys. A Solids Surfaces* **1985**, *38* (4), 275–279. https://doi.org/10.1007/BF00616063.

(38) Vogt, C.; Groeneveld, E.; Kamsma, G.; Nachtegaal, M.; Lu, L.; Kiely, C. J.; Berben, P. H.; Meirer, F.; Weckhuysen, B. M. Unravelling Structure Sensitivity in CO_2 Hydrogenation over Nickel. *Nat. Catal.* **2018**, *1* (2), 127–134. https://doi.org/10.1038/s41929-017-0016-y.

(39) Chen, Y.; Qiu, B.; Liu, Y.; Zhang, Y. An Active and Stable Nickel-Based Catalyst with Embedment Structure for CO_2 Methanation. *Applied Catalysis B: Environmental*. 2020, p 118801. https://doi.org/10.1016/j.apcatb.2020.118801.

(40) Bartholomew, C. H. Sintering Kinetics of Supported Metals: New Perspectives from a Unifying GPLE Treatment. *Appl. Catal. A Gen.* **1993**, *107* (1), 1–57. https://doi.org/10.1016/0926-860X(93)85114-5.

(41) Sehested, J.; Gelten, J. A. P.; Remediakis, I. N.; Bengaard, H.; Nørskov, J. K. Sintering of Nickel Steam-Reforming Catalysts: Effects of Temperature and Steam and Hydrogen Pressures. *J. Catal.* **2004**, *223* (2), 432–443. https://doi.org/10.1016/j.jcat.2004.01.026.

(42) Li, Z.; Hu, X.; Zhang, L.; Liu, S.; Lu, G. Steam Reforming of Acetic Acid over Ni/ZrO_2 Catalysts: Effects of Nickel Loading and Particle Size on Product Distribution and Coke Formation. *Appl. Catal. A Gen.* **2012**, *417–418*, 281–289. https://doi.org/10.1016/j.apcata.2012.01.002.

(43) Cui, Y.; Xu, H.; Ge, Q.; Wang, Y.; Hou, S.; Li, W. Structure Sensitive Dissociation of CH_4 on $Ni/\alpha\text{-}Al_2O_3$: Ni Nano-Scale Particles Linearly Compensate the Ea and Ln A for the CH_4 Pulse Kinetics. *J. Mol. Catal. A Chem.* **2006**, *249* (1–2), 53–59. https://doi.org/10.1016/j.molcata.2006.01.009.

(44) Xu, M.; Lopez-Ruiz, J. A.; Kovarik, L.; Bowden, M. E.; Davidson, S. D.; Weber, R. S.; Wang, I. W.; Hu, J.; Dagle, R. A. Structure Sensitivity and Its Effect on Methane Turnover and Carbon Co-Product Selectivity in Thermocatalytic Decomposition of Methane over Supported Ni Catalysts. *Appl. Catal. A Gen.* **2021**, *611*, 117967. https://doi.org/10.1016/j.apcata.2020.117967.